Seismogenic potential of the High Durance Fault constrained by 20 yr of GNSS measurements in the Western European Alps

Marguerite Mathey, Andrea Walpersdorf, Christian Sue, Stephane Baize, Aline Déprez

Geophysical Journal International

Geophys. J. Int. (2020) **222,** 2136–2146
Advance Access publication 2020 June 15
GJI Geodynamics and Tectonics

doi: 10.1093/gji/ggaa292

Seismogenic potential of the High Durance Fault constrained by 20 yr of GNSS measurements in the Western European Alps

M. Mathey,[1] A. Walpersdorf,[1] C. Sue,[1,2] S. Baize[3] and A. Deprez[1]

[1]*CNRS, IRD, IFSTTAR, ISTerre, University Grenoble Alpes, University Savoie Mont Blanc, 38000 Grenoble, France. E-mail: marguerite.mathey@univ-grenoble-alpes.fr*
[2]*CNRS-UMR 6249, Bourgogne-Franche-Comte´ University, 25000 Besançon, France*
[3]*IRSN, PSE-ENV/SCAN/BERSSIN, BP 17, F-92262 Fontenay-aux-roses, France*

Accepted 2020 June 5. Received 2020 June 5; in original form 2020 January 24

SUMMARY

Due to the steady moderate seismicity observed along the Briançon seismic arc, in the south-western French Alps, three temporary GNSS (Global Navigation Satellite System) surveys took place in 1996, 2006 and 2011, across a ∼50 × 60 km^2 wide area, to investigate the surface deformation field. The horizontal velocity field computed from these three surveys showed an east–west extension in the network. A fourth campaign was led in 2016, creating a 20 yr observation span, resulting in measurements which reach a sufficient accuracy to assess whether extension found within the Briançon network is localized onto any particular tectonic feature. Several faults in this area are known to be active normal faults. Assessing the localization of the deformation may lead to a better understanding of the active tectonics of the Alpine belt. To address this issue, a robust velocity field was computed from the combination of the different campaign and permanent GNSS data. Strain rate tensors were derived for the first time in this area on a 0.1 × 0.1 deg grid to assess the distribution of the deformation. The regional deformation appears localized in the Briançon area and reaches up to 20 ± 5 nanostrain yr^{-1} in the centre of the network. The observed velocities were projected on a profile across the network and compared with modelled interseismic deformation to characterize the behaviour of the major active faults known in the study zone. While a two-fault model provides the best fit to the data, a single fault model has only marginally higher residuals, with parameters which are more consistent with the seismotectonics of the region. The localization of the single modelled fault is consistent with the location of the High Durance Fault (HDF). Therefore, we used the known geological location of this structure as *a priori* information in a block model to compute a fault slip rate at the interface between the two blocks. The velocities on the interface indicate 0.4–0.5 mm yr^{-1} of extension, and therefore strain accumulates along the HDF throughout the seismic cycle. The geodetically derived fault slip rate is converted into an equivalent seismic moment release rate, which is consistent within its uncertainty bounds with the known historical and instrumental seismicity of the Briançon area.

Key words: Geodetic instrumentation; Transient deformation; Seismicity and tectonics; Continental tectonics: extensional; Dynamics and mechanics of faulting; Neotectonics.

1 INTRODUCTION

The Western Alps are one of the most seismically active areas of France (Fig. 1a). Due to its regular moderate seismicity, it was one of the first areas instrumented with GNSS in Europe (Chéry *et al.* 1995). The Western Alps thus provide an exceptional long time span of permanent and survey GNSS data. The first stations of the RENAG network (French national permanent GNSS network for research purposes, RESIF 2017) were installed in the French Alps' region in the late 1990s. Four temporary surveys took place in the southern part of the Briançonnais seismic arc, in an exceptionally dense network, during the summers of 1996, 2006, 2011 and 2016. The first three surveys, combined with permanent GNSS (Fig. 1b) data, revealed a deformation pattern with an east–west extension in the network (Walpersdorf *et al.* 2015). This geodetic strain rate tensor is in agreement with some of the kinematic models derived for the Adriatic–Eurasia relative plate motion, which localize the westernmost plate boundary of the Adriatic microplate in the south-western Alps (Calais *et al.* 2002; d'Agostino *et al.* 2008). However, plate tectonics cannot be the sole origin of the deformation in the

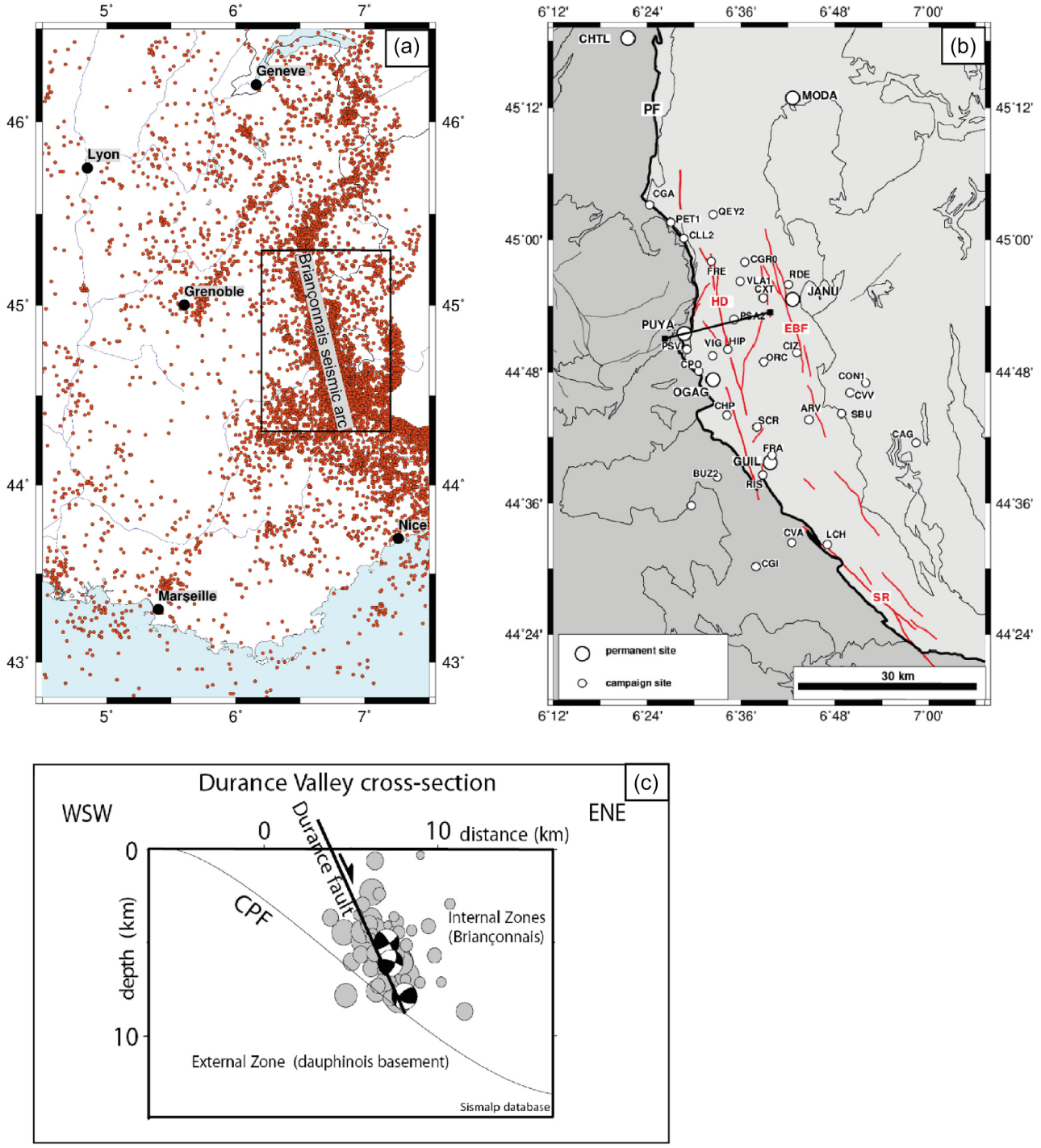

Figure 1. Location map and tectonic context of the study area. (a) Seismicity of south eastern France from FCAT-17 between 1965 and 2009 (Manchuel *et al.* 2018). (b) Major faults in the Briançon area modified from Sue & Tricart (2003): PF = Penninic Front, HD = High Durance Fault, EBF = East Briançonnais Fault and SR = Serennes Fault. Geological units are shown by thin grey lines: dark grey areas = external zones, light grey areas = internal zones. Black line is the location of the cross-section (c) vertical cross-section of the seismicity showing three extensional focal mechanisms and uncharacterized events (grey circles), as well as main faults (CPF = Penninic Front), modified from Sue & Tricart (2003).

Western Alps, as uplift is also observed in addition to extension, as noted by several studies (Delacou *et al.* 2005; Champagnac *et al.* 2007; Vernant *et al.* 2013; Nocquet *et al.* 2016, Walpersdorf *et al.* 2018, Sternai *et al.* 2019). The mechanisms driving the vertical motions in the Western Alps are still debated, and are probably associated with processes operating over longer wavelengths than the network under consideration here. They are thus beyond the scope of this paper.

The present study focuses on the horizontal component of the deformation field to better constrain the active tectonics of the area. We seek to analyse the motion of one or two local faults that could play a major role in the regional tectonics. The fourth campaign, led

in 2016, results in a 20-yr span of observations. The measurements have now reached a sufficient accuracy to precisely assess on which tectonic structures the regional deformation is accommodated. The final objective of our study is to estimate slip rates for these faults, and compare the corresponding rate of geodetic moment release with that estimated from the seismicity catalogue. Such a comparison can be used to develop seismic hazard assessment models, in particular in the context of low-strain continental interiors such as in the Western Alps, which feature low levels of seismicity and long return periods.

2 TECTONIC SETTINGS

The Alps formed in response to the collision between Europe and Africa, which began in the Late Cretaceous. In the Western Alps, the Penninic Front, active during the Oligocene (Tricart 1984), is nowadays the major feature related to this episode. This former thrust fault strikes roughly north–south through the range, dividing it into the so-called 'internal' and 'external' zones. The external part consists of crystalline massifs and their Mesocenozoic cover (belonging to the European margin), while the internal zone is made of metamorphic sheets derived from the Briançonnais microcontinent (Stampfli *et al.* 2002), and the remains of the Ligurian ocean (Schwartz *et al.* 2012). Sue and Tricart (1999) and Sue *et al.* (1999, 2007a) show that this major thrust fault has been reactivated as a normal fault, with smaller normal faults locally connected to it at depth (Sue & Tricart 2003; Tricart *et al.* 2006). This extensional inversion, and associated normal faults, is still seismically active (Sue *et al.* 1999; Sue & Tricart 2002; Delacou *et al.* 2004). Seismicity and deformation are indeed persistent (although weak) across the Western Alps despite the end of Europe-Africa collision (e.g. Delacou *et al*. 2004, 2008).

The Briançon GNSS network area is located in the south-western French Alps and represents a 50 × 60 km^2 wide area straddling the internal and external parts of the chain. The area is characterized by structures belonging to two major tectonic episodes (Sue & Tricart 2003). The first set of faults includes fold and thrust structures which date from Oligocene time, when the internal zones were thrust onto the external zone along the Penninic Front. These structures are overprinted by a second transtensive phase of deformation (Neogene-present), resulting in Late Alpine faulting within the internal zones of the arc. The major faults of this episode in the Briançonnais area include the High Durance fault (HDF), running roughly north-south, and the Serennes fault (SF), which is a continuation of the HDF (Fig. 1b). The East Briançonnais Fault (EBF) is a secondary, shorter fault, located east of the HDF and is less well documented. The HDF is a normal fault, and may be connected at depth to the Penninic Front, which is also actively extending (Sue & Tricart 2003; Sue *et al.* 2007a), while the EBF may be associated with a dextral strike slip regime (Sue & Tricart 2003). Both faults have steep dips to the east (∼60°–80°), deduced from their surface structural expression, and microseismicity focal mechanisms (as shown for the HDF in Fig. 1c).

3 GNSS DATA ANALYSIS

A temporary GNSS network of 30 stations (Fig. 1b) was installed in 1996 in an area of 50 × 60 km^2 using classical 'bolt marks' (Sue *et al.* 2000). The corresponding antenna setup is a tripod with an optical tribrach. Forced centring markers (screw marks) were installed in 2006 near each of these original sites. Screw marks were drilled into bedrock, thus allowing installation of an observation mast, which provides forced centring of the antenna. This type of marker creates fewer setup errors compared to classical markers, which need a vertical adjustment of the antenna. A full measurement campaign took place on the classical marks in 1996 and 2016, while the screw marks were reoccupied in 2006, 2011 and 2016. Additionally, in 2006, short measurements were made on the classical marks in order to establish local ties between the old and new monuments.

In addition to these campaign surveys, the French RENAG permanent network (RESIF 2017, http://renag.resif.fr) provides a good spatial coverage of the French Alps. About 40 stations were installed and measured since 1998 covering the entire Western Alps. Six stations of this national network lie in the Briançonnais area (Fig. 1b). These six stations were installed between 1998 and 2011.

At a larger spatial scale, 36 IGS (International GNSS Service) stations were included in our analysis to constrain the stabilization frame (ITRF2014, Altamimi *et al.* 2016). The stabilization stations have been selected depending on their observation span and geographical location.

Daily positions of the stations are computed with the GAMIT/GLOBK software (Herring *et al.* 2015). The data are processed using double differences, with precise IGS orbits and up-to-date ocean and atmospheric loading models (Tregoning & Van Dam 2005; Lyard *et al.* 2006), as well as tropospheric mapping functions and *a priori* values (Vienna Mapping Function version 1, Böhm *et al.* 2006).

The velocities were estimated using the Kalman filter GLOBK. To evaluate meaningful velocity uncertainties, the real sigma strategy has been applied (Reilinger *et al.* 2006). This strategy evaluates the amount of Markov noise individually for the three position components of each of the permanent stations. A conservative amount of Markov noise was attributed to the survey stations with 4 and 8 mm^2 yr^{-1} on the horizontal and vertical components, respectively (Vernant *et al.* 2004). The uncertainties output by GLOBK on the velocity estimates depend mostly on the amount of Markov noise attributed to the stations. Therefore, the uncertainties of campaign sites are systematically larger than permanent sites, while otherwise both campaign and permanent site uncertainties depend mostly on the time span of instrumentation of the site (Supporting Informations 1 and 2).

The stabilization frame ITRF2014 is defined by 36 IGS stations. Horizontal velocities are calculated with respect to stable Eurasia by determining the rigid plate motion using 46 Eurasian stations. The Euler pole for the Eurasian plate with respect to ITRF2014 is found at 55.378 ± 0.176°N and −97.946 ± 0.387°E with a corresponding rotation rate of 0.263° My^{-1} (Cartesian rotation components and their covariance are available in Supporting Information 2), which is consistent with previous studies (Walpersdorf *et al.* 2015; Altamimi *et al.* 2016). The resulting velocity field and their uncertainties are presented and discussed in the following Section 4.

4 RESULTS

4.1 Velocity field

Thanks to the long observation span, almost all horizontal site velocities have converged to values below 1 mm yr^{-1}, which was considered as a velocity threshold for tectonic significance in this slowly deforming region (Walpersdorf *et al*. 2015, 2018; Nguyen *et al.* 2016; Nocquet *et al.* 2016). Exceptions are sites RES, CVV,

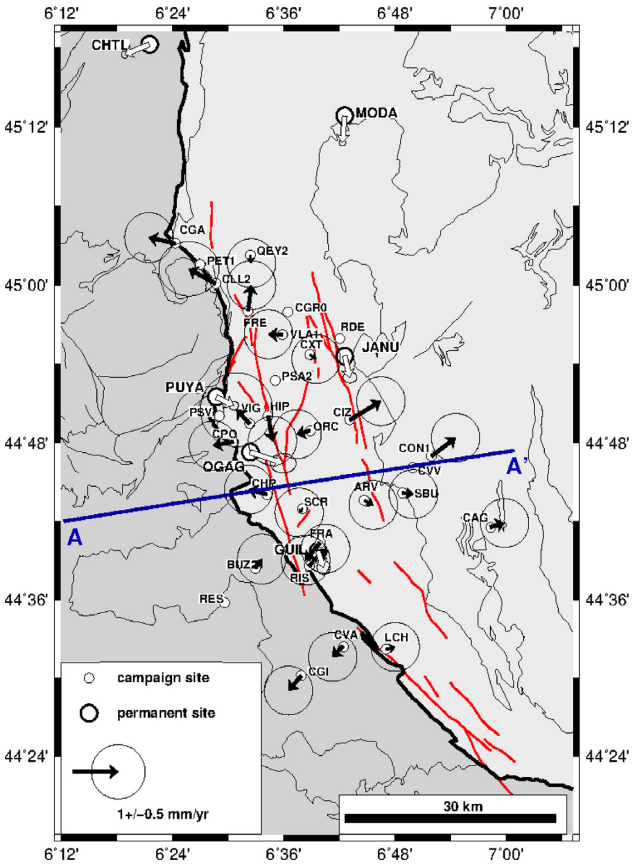

Figure 2. Velocity field with respect to Eurasia obtained by the local tie solution (black vectors). White vectors are the permanent stations located within the Briançon network. GPS velocities are projected on profile AA′ (see Section 4.3 for details). See Fig. 1 for underlying geological units and fault traces.

PSA, CGR, PET, PSV and RDE with velocities at least one and a half-times higher than the maximum expected tectonic signal. Field investigations confirmed that they were not installed on bedrock. These stations were thus excluded from the velocity field presented in this study.

The processed GNSS data set combines measurements made over 20 yr (for the bolt markers installed in 1996), and 10 yr (for the forced centring markers), together with local tie measurements between the two benchmarks of each site. Given the richness of the measurements, which display a high degree of redundancy, we conduct methodological tests to identify the optimal use of the final data set. These tests, based on a dispersion criterion of the velocities (Pinget 2016), are presented in Supporting Information 3. The results indicate that the most coherent velocity field combines the velocity derived from (1) two campaigns on the old markers (1996 and 2006), and (2) three campaigns on the new markers (2006, 2011 and 2016). This solution uses the local tie data of 2006 and excludes the position data of the 2016 survey on classical bolt marks. This velocity field, shown in Fig. 2, identified in the tests as the 'local tie solution', forms the basis of the following analysis.

The velocity amplitudes with respect to stable Eurasia range from 0.2 to 0.9 mm yr^{-1}. The uncertainties are $\pm$0.45 mm yr^{-1} for campaign sites instrumented during four surveys. The uncertainties are higher for several sites that were not instrumented during each survey, such as VIG1 ($\pm$0.8 mm yr^{-1}). The uncertainties of the permanent stations range from $\pm$0.06 mm yr^{-1} for MODA (which is the oldest station of the network) to $\pm$0.25 mm yr^{-1} for OGAG (which is the youngest).

The velocity field reveals a coherent pattern. The majority of the stations located west of the HDF are moving westward, while those to the east are moving eastward. This pattern was a feature of the velocity field previously derived by Walpersdorf *et al.* (2015). With respect to this preliminary solution, our velocity field is more coherent, with only PUYA, OGAG, VLA1, ORC and SCR not following this pattern. Also, the general northward motion previously seen for the campaign stations, and which was thought to result from limited ties between the classical and the new markers, is now attenuated following inclusion of the 2016 measurements. Based on the observation of a general east-west extension in the network, and on the evidence of the HDF being the major active fault in the region (see Section 2), we make the basic first-order hypothesis that the regional deformation is dominated by the relative extensional motion of two tectonic blocks separated by the HDF. We use this hypothesis as a criterion to evaluate the quality of the different velocity solutions. We computed the average absolute deviation to the mean velocity on each side of the fault (Supporting Information 3), and used this dispersion measurement to classify the velocity solutions. For the 'local tie' solution, the dispersions of the east and north velocity components are 0.06 and 0.08 mm yr^{-1} on the western block, and 0.03 and 0.18 mm yr^{-1} on the eastern block. The dispersion on each side of the main active fault is small, thereby supporting our initial hypothesis that deformation of the Briançonnais region is well characterized by two blocks along the HDF.

4.2 Strain rate field

The evaluation of strain rate tensors allows us to further analyse the deformation field, since they make use of redundancies between nearby stations. Large-scale geodetic strain rate fields have been successfully derived from permanent stations throughout the Western Alps (Walpersdorf *et al.* 2018) and Europe (Sanchez *et al.* 2018). Both studies confirm the extension in the Briançon area that has previously been reported (Walpersdorf *et al.* 2015). Our study aims at exploiting the enhanced precision brought by the re-measurement of the dense local network in 2016, with the aim of increasing spatial resolution of the strain rate field, thereby allowing us to better characterize the zone of extension inside the Briançonnais region. For that purpose, the strain rate field will be used to validate our initial hypothesis of two microblocks separated by an active fault (the HDF).

The first strain rate introduced here corresponds to a single rate for the entire local network. It reveals (1) an east–west extension rate of 20 ± 2 nanostrain yr^{-1} (azimuth of $118 \pm 3^{\circ}$ from north), equivalent to a velocity difference of 2 mm yr^{-1} over 100 km, and (2) a smaller north–south compressive component of 8 ± 2 nanostrain yr^{-1}. This strain tensor is consistent with the one determined by Walpersdorf *et al.* (2015), yielding an extension rate of 16 ± 8 nanostrain yr^{-1}.

Our data are too noisy, with respect to the weak total deformation, to determine strain rates based on a simple triangulation method (e.g. Delaunay triangulation, Shewchuk 1996). Therefore, we applied a smoothing filter between nearby stations of the network to estimate the strain rate tensors. The baseline length variation approach uses the distance changes between all pairs of stations (Masson *et al.* 2014). This strategy reduces the dependency on a single station's velocity with respect to the neighbouring stations by cumulating the deformation of all baselines where they cross a grid cell. The impact of an outlier velocity at one station is thus

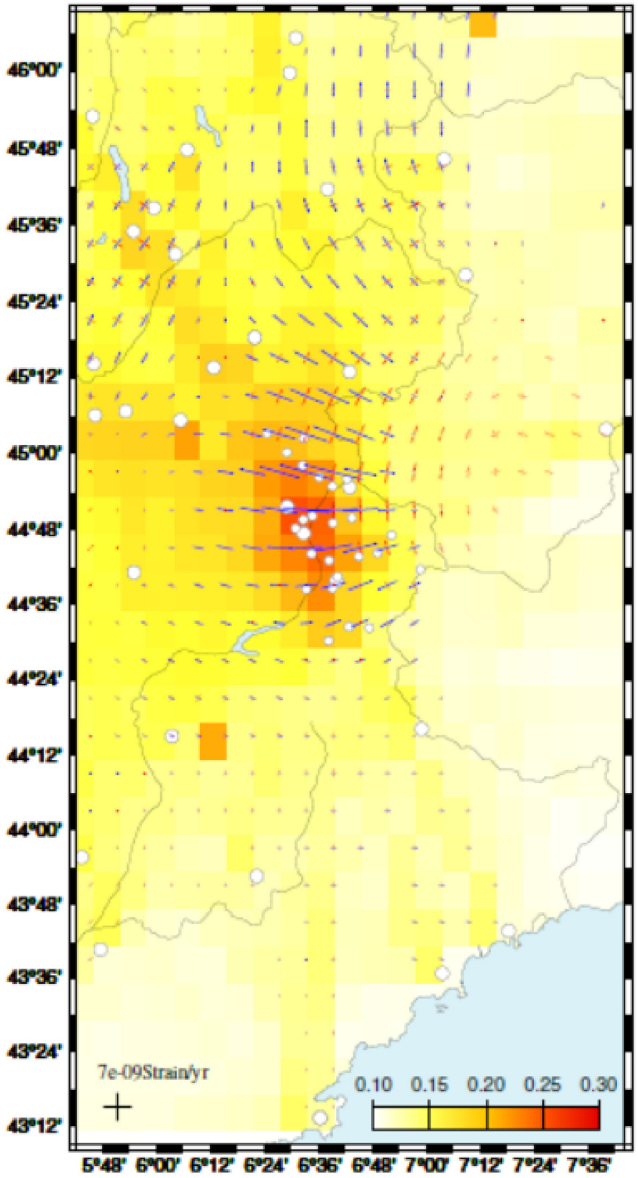

Figure 3. Strain rates in the Western Alps, based on permanent and survey GPS station velocities. Extension = blue arrows, compression = red arrows. Circles = permanent and survey GPS stations. Cells of $0.1^\circ \times 0.1^\circ$ are coloured according to the model resolution of the strain rate (dimensionless criterion, defined in Masson *et al.* 2014).

reduced, and does not create an inaccurate local strain patch. In our study, horizontal strain rate tensors are estimated from variations in geodetic distance ('baseline length') using this STIB code (Masson *et al.* 2014). To do so, we embed our study area in a much larger one (from 3° to 10°E and 41° to 49°N , Fig. 3). The strain tensors are computed on a $0.1^\circ \times 0.1^\circ$ grid, with a constant 15 km smoothing distance throughout the network. The accuracy of the model is given through the diagonal term of the model resolution matrix in each cell (color density in Fig. 3).

The strain rate field confirms the existence of an E-W extension pattern spread over the whole campaign network. The extension amplitude decreases north of our area and turns to a more N-S orientation, coherent with both the geodetic analysis by Walpersdorf *et al.* (2018) and the overall seismotectonic framework (Sue *et al.* 1999; Delacou *et al.* 2004). The maximum extension is found in the centre of the local Briançon network on the cells of 44°51′ N. Strain rate tensors summed between 6°24′ and 7°E on this parallel reach 23 nanostrain yr^{-1}. However, the extension is distributed over the whole network and thus is not localized within a single cell. The model resolution, given by the diagonal term of the resolution matrix in each cell (Masson *et al.* 2014), depends mainly on the density and distribution of the baselines crossing the cell. This dimensionless quantity ranges from 0.12 to 0.27 in our network, and decreases below 0.1 in the other parts of the map. Only tensors having a resolution term over 0.1 are shown in this strain field. Following Masson *et al.* (2014), who propose a more conservative value of 0.5 as a minimum threshold while applying STIB to a more actively deforming area, we acknowledge that one must be careful when interpreting our results.

4.3 Localization of the deformation on a velocity profile: elastic dislocation modelling

An alternative method is to investigate the localization of the extensional motion by fitting the surface velocities by a dislocation model (Segall 2010). This modelling method has recently been used in various deformation contexts (e.g. Mousavi *et al.* 2013; Daout *et al.* 2016; Mariniere *et al.* 2019). This first-order approach considers a screw dislocation propagating along an infinite buried line to model interseismic locking on a dip-slip fault.

The velocities along the profile are predicted by the following equation:

$$Vmod = -\frac{s}{\pi}\left(\cos\delta\left(\tan^{-1}(\zeta) - \frac{\pi}{2}\,\mathrm{sgn}(x)\right) + \frac{\sin\delta - \zeta\cos\delta}{1+\zeta^2}\right)$$
$$\text{where } \zeta = \frac{x - \frac{z}{\tan\delta}}{z} \qquad (1)$$

With:

s = slip on the fault (mm yr^{-1})
x = distance between the modelled velocity and the fault (km)
z = depth of fault bottom (km)
δ = dip of the fault (radians)

We define a fault perpendicular profile AA′ (Fig. 2) in the centre of the dense campaign network. We then project all station velocities (except the most distant ones: CHTL, MODA, CGI, CVA and LCH) onto this profile, to retrieve fault-perpendicular velocities. Models are computed investigating every possible combination of the four following parameters:

(i) longitude of surface trace varying between 6.4° and 7.5° with 0.1° steps in longitude;
(ii) dip varying from 20° to 90° with 1° steps;
(iii) slip rate varying between 0 and 2 mm yr^{-1}, in 0.1 mm yr^{-1} steps; thus we explore three fault models: no faults (both slip rates equal 0), one fault (one slip rate equals 0 and the other > 0), or two faults (both slip rates > 0);
(iv) locking depth varying from 0 km for free-slipping faults to 15 km.

This parametric study provides constraints on the geometry of the fault as well as its location.

The depth of the bottom of the fault is fixed to 300 km in order to model an infinite fault. For each model, the root mean square (rms) residual is computed between the observed projected velocities and the modelled velocities:

$$\mathrm{rms} = \sqrt{\Sigma\frac{(Vobs - Vmod)^2}{N}} \qquad (2)$$

Where:

Vobs = observed fault perpendicular velocity component at one station
Vmod = modelled fault perpendicular velocity at one station
N = number of stations

As explained in Section 3, formal uncertainties associated with each station velocity may not be representative, especially for survey stations. Thus we do not take into account velocity uncertainties, which amounts to an equal weighting of all stations. The model showing the smallest rms is considered as the best-fitting model (Fig. 4).

We tested models with a single or two dislocations to compare the effect of one or two faults, respectively. The model computed for a single fault (dashed curve in the upper part of Fig. 4, and black line in the lower part) yields an rms value of 0.27 mm yr^{-1}. The best-fitting single-fault model is located 35 km along the profile. The associated parameters (a dip of 55°, a locking depth of 10 km and a slip rate of 1.9 mm yr^{-1}) are consistent with the seismotectonic setting, and indicate a steep fault with a moderate locking depth (Section 2; Sue & Tricart 2003). The two-fault model does not significantly reduce the rms value below that of the single fault model (blue curve in the upper part of Fig. 4, and blue lines in the lower part). Therefore, we only consider the single fault model for our subsequent analysis; this fault represents the HDF, with the associated parameters derived from our unique fault model.

Fig. 5 shows the rms related to the one fault model grid search for a given pair of parameters. Two of the four parameters are free to vary, while the others are fixed to the values deduced from the best-fitting one fault model. Two examples are presented here: (1) varying slip rate with varying location of the fault (Fig. 5a), and (2) varying slip rate with varying locking depth (Fig. 5b). The first plot indicates that the fault longitude is well constrained. The second plot indicates that both fault slip rate and locking depth should increase together for rms values to remain low. However, both plots show that the slip rate of the fault is less well constrained, which may contribute to the relatively high slip rate in the best-fitting fault model.

Our results suggest that the westernmost fault (i.e. the HDF) acts as the major regional structure accommodating most of the measured deformation. This deformation is consistent with interseismic locking, as the observations fit the overall shape of a profile expected for a locked fault.

However, while our forward modelling highlights the variability and correlation between the different fault parameters, the amount of horizontal extension remains poorly constrained, probably due to block rotations which are not taken into account on the velocity profile. We therefore apply a complementary block rotation model based on our single fault model. Our aim is to estimate the fault slip rate that takes into account the rotation of tectonic units each side of the fault.

4.4 Fault slip rate estimates: block model

We use a block model approach to reassess the horizontal fault slip velocities, following the approach of McCaffrey (2009, based on the DEFNODE code). The GPS velocity field is interpreted within the context of the regional tectonic framework, that is active faults separating non-deforming blocks, the motion of which are described by rotations about their Euler poles. This approach allows an evaluation of the fault slip rate for the various faults in the model. The deformation field at the block boundaries due to fault locking is computed using the back-slip approach (Segall 2010). This strategy has the advantage that fewer parameters need to be tested compared with the elastic dislocation model.

Two blocks are defined at each side of the geological surface trace of the HDF. Fig. 6 shows the limits of the blocks used, with the observed GPS velocities in Fig. 6a and the velocities predicted by DEFNODE at each GPS site in Fig. 6b. The borders of the blocks which are not the HDF are slip freely. The computed velocities include the block rotation, plus a back-slip contribution due to interseismic fault locking close to the fault. The locking depth is here imposed (to prevent solving an underdetermined problem). The locking is constant along the strike. The interface is fully locked from 0 to 10 km and freely slipping below 10 km, the maximum depth of seismicity in the Briançon area (from seismic catalogues, e.g. FCAT-17, Manchuel *et al.* 2018). However, locking depths of 2, 5, 10, 15 and 20 km were tested and show similar fits to the observations. Stable Eurasia, considered as the reference frame of the computed velocities, is modelled by a block with null velocities west of the system.

The Euler poles describing the two block motions are found at 6.7°E, 43.9°N for the western block and 6.9°E, 45.2°N for the eastern one, with rotation rates of 0.16 ± 0.3 and 0.33 ± 0.4 ° My^{-1}, respectively. The values of the relative horizontal velocities perpendicular to the limit between the two blocks vary from 0.4 to 0.5 ± 0.3 mm yr^{-1}. These velocities correspond to the extensional component of the deformation. The model also gives a smaller, fault parallel, dextral strike-slip component of 0.1 to 0.2 ± 0.3 mm yr^{-1} along the fault.

The normalized rms between modelled and observed (Fig. 6a, observed velocities from local tie solution, see Section 4.1 and Fig. 2) GPS velocities at each station reaches 0.560 mm yr^{-1}. The predicted velocities are small compared to the observed ones, but are nevertheless consistent with an E-W extension at plausible rates in this area of slow deformation.

The Euler poles, and therefore the predicted fault slip rates, are strongly dependent on the model parameters, such as the locking ratio (ratio of locked to total width of the fault), and uncertainties in GPS velocities. In particular, the software fits Euler poles to the stations with the smallest uncertainties. Therefore, the modelled velocities presented in Fig. 6b have been obtained by weighting equally each observed GPS velocity (in particular weighting equally both permanent and campaign stations).

To evaluate the impact of fault locking, we run the same block modelling with a freely slipping fault. In this case, DEFNODE solves only for the block rotations. The total velocity at the freely slipping interface between the two blocks is 0.2 to 0.3 ± 0.2 mm yr^{-1}. The normalized rms for this model is 0.628, which is higher than with fault locking. While the model fit cannot distinguish between different locking depths, it still favours a locked rather than a freely slipping fault interface.

The residuals remain high largely because of noise in the data, which is somewhat attenuated by the fourth survey (after 20 yr), but nevertheless still persistent. This noise is mainly due to the different motions of the permanent stations with respect to the survey stations. These differences may be explained both by the different time spans of observation leading to reference frame issues, and by the individual geological units in which the stations are located. Although we identified several outlier stations that were removed due to site

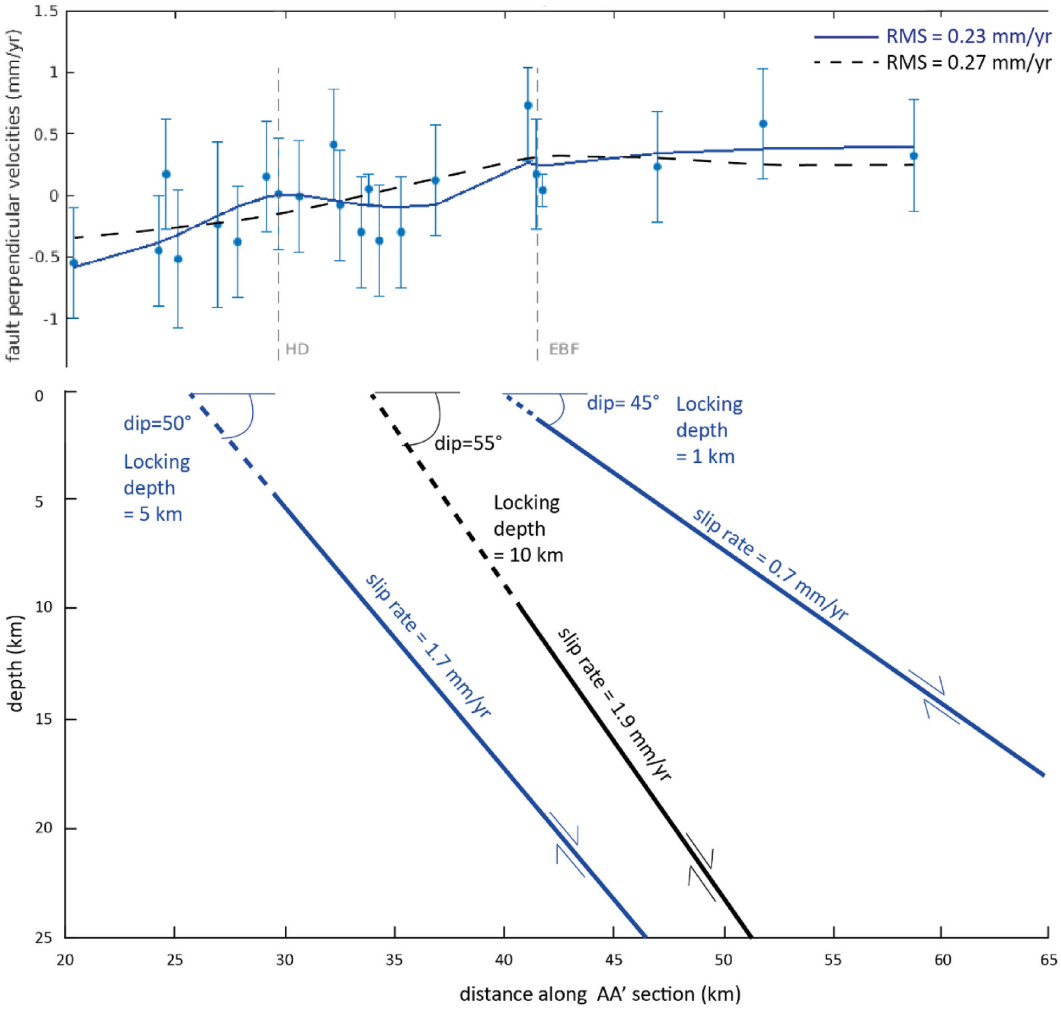

Figure 4. Upper plot: best-fitting one-fault (dashed curve) and two-fault (blue curve) models corresponding to the observed velocities (blue dots). Grey dashed lines mark the emplacement of surface geological evidence of the HDF and EBF, respectively. Lower plot: fault locations, dips and slip rates are indicated by black (one-fault model) and blue lines (two-fault model). *X*-axis indicates the distance along the profile AA′ (location shown in Fig. 2). *Y*-axis shows the fault-perpendicular projected velocity in mm yr^{-1} (upper plot), and depth (bottom plot).

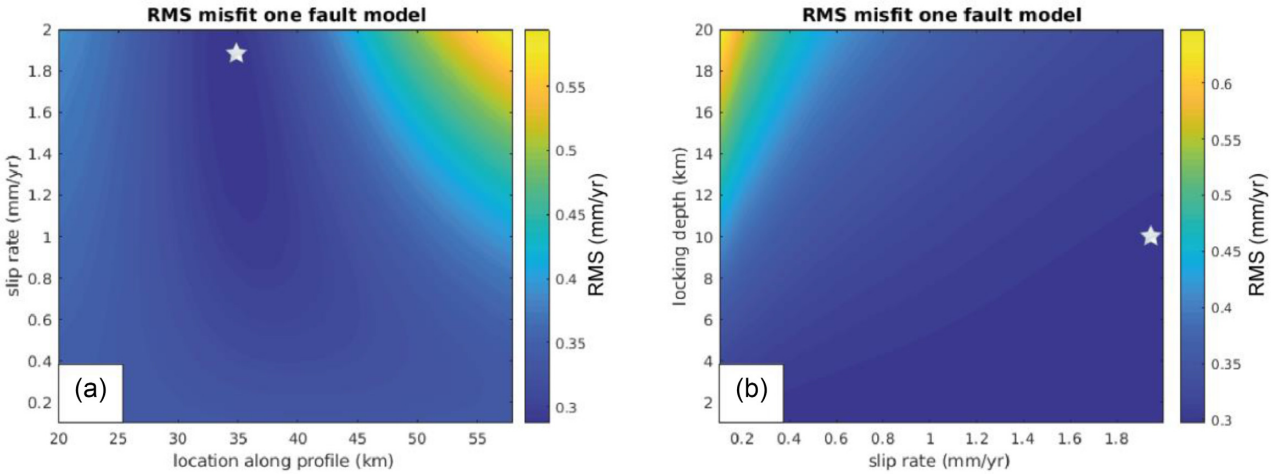

Figure 5. Grid search of the rms residual of the best one fault model for two parameters varying together: (a) slip rate of the fault varying from 0 to 2 mm yr^{-1}, location of the fault at the surface varying from 20 to 60 km along AA′ profile (Fig. 2), all other parameters fixed; and (b) slip rate of the fault varying from 0 to 2 mm yr^{-1}, locking depth varying from 0 to 20 km, all other parameters fixed. Stars indicate parameter values retrieved from the preferred one fault model (Fig. 4).

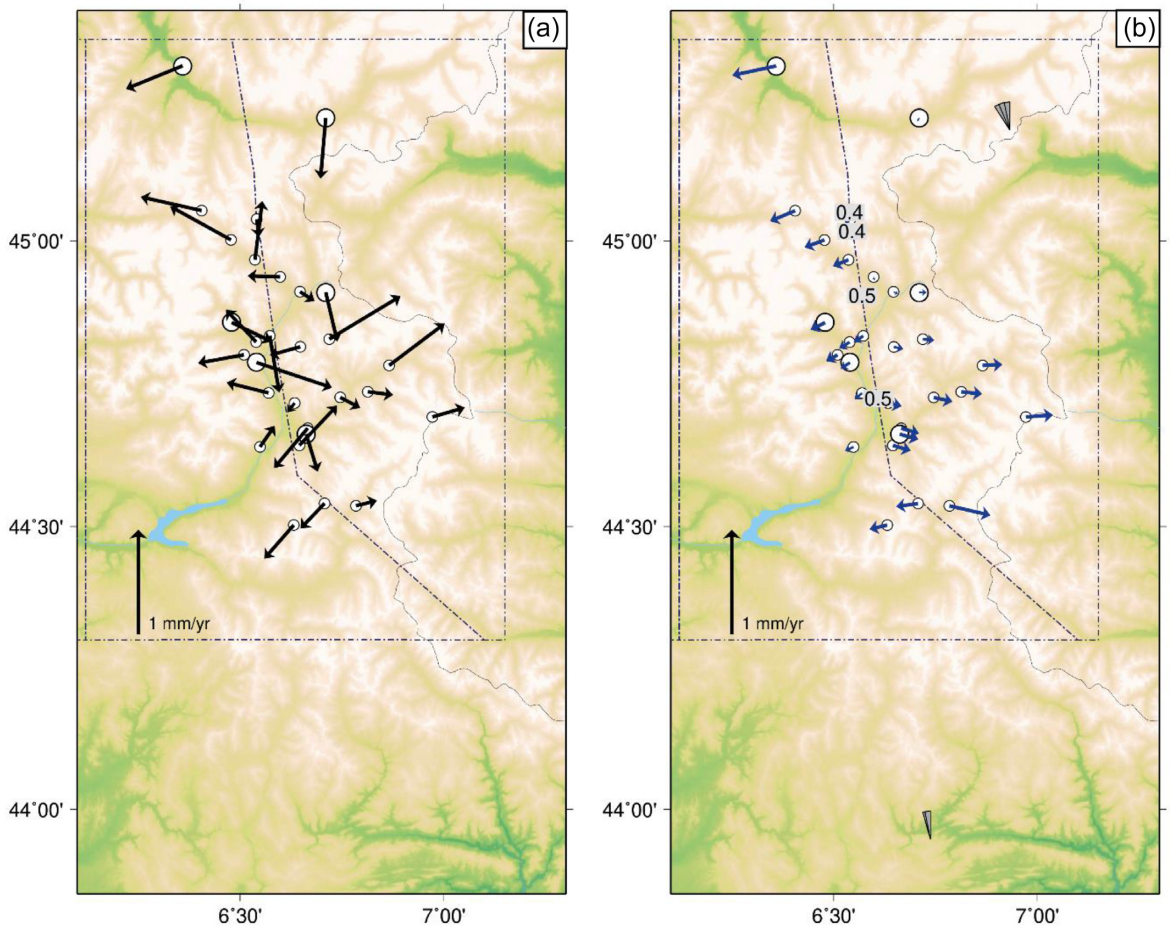

Figure 6. Block model. Dashed blue lines define the block limits. The line between the two blocks represents the HDF. Values along the interface give the computed fault velocity (fault perpendicular, extensive component) in mm yr^{-1}. (a) Observed GPS velocities from the velocity field identified as the best solution (local tie solution, see Section 4.1 and Fig. 2). (b) Velocities computed from the model accounting for both block rotation and interseismic fault locking. The Euler poles of each block are represented by grey fans (upper one for the eastern block and lower one for the western block).

instabilities (Section 3), some additional corrupted stations likely remain in our analysis; stations which are subject to slope instabilities at velocities similar to the tectonic motion. Indeed, the study of the time-series show that there is no random noise associated with the unstable stations. This slope instability bias may therefore affect survey as well as permanent stations. Thus, if some stations measure a gravitational phenomenon at velocities close to the expected tectonic signal, we are unable (through GLOBK processing) to distinguish between stations valid for tectonic interpretation, and ones that are not.

Despite the scatter between the velocities estimated for survey and permanent stations, extension is found to be the principal slip component along the fault HDF interface, along with a minor component of right-lateral strike-slip. The block modelling takes into account more GPS station velocities than elastic dislocation modelling along a profile. In addition to evaluating the extent of fault locking while also considering block rotations, block modelling also enables us to derive complete slip rates on the fault, which take into account both strike-slip and dip-slip components. The residuals remain high; however the retrieved slip rates are consistent with the expected tectonic signal. Eventually, we estimate that the uncertainties on the geodetic slip rates are coherent with the lower bound of the seismic potential of the HDF based on its historical seismicity (Section 5.2).

5 DISCUSSION

5.1 Resolution limits of strain rate fields

The first part of our work consisted in assessing whether the deformation in the Briançon region was distributed or localized onto a specific fault. Strain rate estimation using the STIB method (Section 4.2) did not enable us to identify the location of any particular fault. However, the general pattern is in good agreement with larger scale strain fields, such as the one evaluated by STIB on the Western Alps (which includes the same permanent data as in our computation, see Walpersdorf *et al.* 2018). In the large-scale strain field ($0.5^\circ \times 0.5^\circ$ grid) of Walpersdorf *et al.* (2018), extension is localized in our study area, with the diagonal term of the resolution matrix larger than 0.5 in the cells encompassing the Briançon area. The change of scale from a regional to a local network appears to be difficult to realize with the STIB software, which is limited to the use of a constant smoothing distance throughout the network.

As the GPS stations are not equally distributed over the area, allowing the smoothing distance to vary may reduce the uncertainties, while increasing both spatial and model resolution. We therefore implemented another strain rate computation software (VISR, from Shen *et al.* 2015) to compute strain rates based on a smoothing distance which depends on the density of stations in the vicinity

of a given cell. However, no sufficient model resolution could be reached in each individual cell.

One explanation for the difficulty to establish a high spatial resolution strain rate field is that the dense local velocities are slow and not yet coherent enough to constrain a relevant strain rate field over the short distances in our network. Indeed, over distances below a few hundred meters, the resolution of individual velocity estimates must be still better than the one obtained by 10–20 yr of campaign measurements, or some 10 yr of permanent data (of the order of 0.2 mm yr^{-1}, Tarayoun 2018). Given the strain rate value is a difference of velocities integrated over a given distance, the signal-to-noise ratio is still too low inside the width of our network (∼50 km).

5.2 Implications of geodetic slip rate on seismogenic potential

The next part of our study (elastic modelling on a profile, Section 4.3) has shown that the GPS observations in the Briançon region are most compatible with the existence of a single active fault at the location of the HDF. Assessing the distribution of the deformation around a given fault by block modelling (Section 4.4) enables us to evaluate a range of possible slip rates along the fault. The best model thus corresponds to values projected along the interface between 0.3 and 1.4 mm yr^{-1} of total slip rate, which takes into account both fault-parallel and fault-perpendicular components (and their uncertainties), with a locking depth of 10 km (consistent with seismic catalogues and compatible with the GPS observations). Interseismic slip rates on faults and associated locking depths can be a useful input to quantify the hazard related to a specific fault or to a fault network. The relatively shallow locking depth of 10 km retrieved from seismic catalogues and consistent with GPS velocities could suggest low-to-moderate moment accumulation. This value, along with the estimated slip rate of the fault, can be used to compute a geodetic equivalent moment rate (e.g. Brune 1968; Ward 1994):

$$\dot{\mathrm{Mo}} = \mu \, \mathrm{s} \, \mathrm{A} \tag{3}$$

Where μ is the rigidity modulus in $N{\cdot}m^{-2}$, s is the slip rate in m yr^{-1} and A is the locked area of the fault in m^2.

The area depends on the length of the segment along-strike that is considered capable of rupturing in a single event. Assuming a single-segment rupture scenario, and taking into account the longest segment of the fault, we consider a rupture length of 30 km. (We do not investigate the effect of uncertainties on μ or maximum A, which falls into the scope of seismic hazard assessment). For this maximum single-segment scenario, and considering a fault rupture area of 30×10 km $= 300 \times 10^6$ m^2; with $\mu = 3.2 \times 10^{10}$ $N{\cdot}m^{-2}$, we obtain a minimum estimate of $\dot{\mathrm{Mo}} = 2.9 \times 10^{15}$ $N \cdot m\,yr^{-1}$(for a slip rate on the fault of 0.3 mm yr^{-1}), and a maximum $\dot{\mathrm{Mo}} = 1.4 \times 10^{16}$ $N \cdot m\,yr^{-1}$(for a slip rate on the fault of 1.4 mm yr^{-1}), considering minimum and maximum values of slip rate respectively, which take into account both along-strike and along-dip components of the slip and their lowest and highest uncertainty bounds, respectively.

The equivalent moment rate accumulated by fault locking can be compared with the actual moment rate released annually in the area based on seismic catalogues. We use the FCAT-17 catalogue (Manchuel *et al.* 2018), which is the first database encompassing both historical and instrumental events for the whole of France. The summation of event moments in a given area, divided by the time span of a given period, allows us to obtain annual seismic moment rates. We compare the geodetic and seismic rates for the same area. First, we summed event moments in the area covered by our local geodetic network, from 6.0° to 7.0°E and 44.3° to 45.3°N. The annual seismic moment rate derived in the area of interest from the FCAT-17 catalogue corresponds to 7.71×10^{13} $N{\cdot}m\,yr^{-1}$ (when only instrumental seismicity from 1965 + is taken into account), which is two orders of magnitude less than the geodetic rate. However, the seismic moment rate reaches 2.67×10^{15} $N{\cdot}m\,yr^{-1}$ if we also consider historical seismicity of the Briançon area. Thus, the moment rate difference can be explained by a few historical events representing most of the moment release. Instrumental seismicity in the area indeed reaches only M_w 3.5, while seven historical events have associated moment magnitudes ranging from 4.3 to 5.6. Therefore, the rate estimate largely depends on the uncertainties on the biggest historical earthquakes. These seven events have a mean magnitude uncertainty of 0.4 (Manchuel *et al.* 2018), with an inversion flag of 3 over 4 (flag 1 corresponding to the less well-constrained inversions, Manchuel *et al.* 2018).

The value of moment per year accounting for both historical and instrumental seismicity is of the same order as the minimum moment rate derived from geodetic slip rates on the modelled HDF. This would suggest that all or the main part of the geodetic deformation measured in the Briançon area could be released by the current seismic activity. The current geodetic deformation could be representative of the mid-term (historical and instrumental) seismicity rate, which corresponds to about one M_w 4 event each year. This result clarifies the comparison between geodetic and seismic strain rates developed by Sue *et al.* (2007b), and reworked by Walpersdorf *et al.* (2015). On the other hand, the discrepancy we obtain between the maximum estimate of moment rate from geodesy and the maximum estimate from seismic catalogues could be representative of the part of aseismic processes measured by geodesy. Another explanation could also stand in the completeness of the historical catalogues, which is not reached before 1625 for $M_w > 5.0$ earthquakes in the region (Hannouz 2019).

Some processes not linked to plate tectonics (e.g. erosion, glacial isostatic adjustment and mantle upwelling) could also induce extension at the surface as well as uplift. It has been proposed that more than one of these processes contributes to the present day uplift and extension of the Western Alps (see review and discussion in Sternai *et al.* 2019). However, there is still no consensus on the relative contribution of each process on the observed uplift values. Given the magnitude of horizontal velocities is one order of magnitude smaller than the vertical velocities, it would be challenging to determine the role of fault loading and far-field plate tectonics with respect to surface and deep intrinsic processes from the horizontal component of deformation.

6 CONCLUSION

This study takes advantage of a dense and highly redundant GPS network in the south western Alps to (1) constrain the strain field of this low deformation region, (2) identify which tectonic structures contribute to the accommodation of regional tectonic motion and (3) characterize the seismogenic potential of active faults in the region.

By incorporating a new (fourth) GPS campaign, we first extend the period of GPS observation in the south western Alps to 20 yr. This considerably increases the spatial resolution of the slow

deformation pattern compared to earlier studies (based on three surveys over 15 yr). The spatial resolution is now good enough to link the strain field to known tectonic structures, and characterize the seismogenic potential of individual faults.

The general pattern of E-W extension was previously identified in the Briançon area by seismotectonic and geodetic studies, albeit without knowing whether the deformation was diffuse or localized onto one or more active faults. Through a combination of different analysis methods, we determine the characteristics of active faulting in the Briançon region. Exploiting redundancy of the GPS velocities in the dense network, we better locate where extensional deformation is accommodated in the region using an elastic dislocation modelling approach. Extension is largely accommodated on a single active N-S trending normal fault. The location and geometry of the fault is consistent with a known geological fault, the HDF, which is a major active structure within a dense network of smaller range-parallel faults located within the eastern French Alps.

We develop a kinematic block model for the region, incorporating the observed velocity field, along with information on known geological structures, to retrieve details on the tectonic behavior of the HDF. Despite substantial slip rate uncertainty, the lower bound of moment accumulation rate predicted for the HDF is found to be consistent with the seismic moment released during the historical and instrumental periods (corresponding to $\sim$1 M_w 4 event each year).

Future re-measurement of the French Alps GPS network will likely yield further improvements in the precision of station velocities, such that both the horizontal and the vertical components will allow a robust assessment of the origin and significance of extension in the Western European Alps. Furthermore, a combined analysis of higher quality horizontal and vertical deformation would also help to address the issues commonly raised in the Alps, such as the way these components are linked, their relative impacts on the current seismicity, as well as the way they are related to the chain's topography and deep structure.

ACKNOWLEDGEMENTS

This work was funded by both the IRSN (Institut de Radioprotection et de Sûreté Nucléaire) and the LabEx OSUG@2020 (Investissements d'avenir - ANR10LABX56). We first thank the Editor, Pr Duncan Agnew, as well as Pr Kurt Feigl and an anonymous reviewer for their constructive comments. We are particularly thankful to James Hollingsworth who was of great help in improving our manuscript. Instruments used during the 2016 GNSS survey were provided by GPSmob, which is a RESIF (Réseau Sismologique et Géodésique Français) targeted action. We would also like to thank all the operators of the 2016 GNSS survey: C. Berthier, M. Deheuvels, A. Déprez, A. Esparel, G. Ferhat, J. Forner, R. Gahéry, G. Gibert, L. Harel, G. Jolain, A. Laurin, E. Lewin, M. Maret, A. Mercier, E. Poirier, A. Potier, A. Replumaz, M. San-Jose, C. Sue, P. Talour and I. Tavel-Besson, without whom this study would not have been possible.

REFERENCES

Altamimi, Z., Rebischung, P., Metivier, L. & Collilieux, X, 2016. ITRF2014: a new release of the International Terrestrial Reference Frame modeling nonlinear station motions, *J. geophys. Res.,* **121,** doi:10.1002/2016JB013098.

Brune, J.N., 1968. Seismic moment, seismicity, and rate of slip along major fault zones, *J. geophys. Res.,* **73**(2), 777–784.

Böhm, J., Niell, A., Tregoning, P. & Schuh, H., 2006. Global Mapping Function (GMF): a new empirical mapping function based on numerical weather model data, *Geophys. Res. Lett.,* **33**(7), doi:10.1029/2005GL025546.

Calais, E., Nocquet, J.M., Jouanne, F. & Tardy, M., 2002. Current strain regime in the Western Alps from continuous Global Positioning System measurements, 1996–2001, *Geology,* **30**(7), 651–654.

Champagnac, J.D., Molnar, P., Anderson, R.S., Sue, C. & Delacou, B., 2007. Quaternary erosion-induced isostatic rebound in the western Alps, *Geology,* **35**(3), 195–198.

Chéry, J., Vigny, C., Meyer, B., Ferhat, G., Anzidei, M., Bayer, R. & Gamond, J.-F., 1995. Global Positionning System network monitors the western Alps, *EOS, Trans. Am. geophys. Un.,* **76**(48), 489–489.

D'Agostino, N., Avallone, A., Cheloni, D., D'Anastasio, E., Mantenuto, S. & Selvaggi, G., 2008. Active tectonics of the Adriatic region from GPS and earthquake slip vectors, *J. geophys. Res.,* **113**(B12), 12, doi:10.1029/2008JB005860.

Daout, S., Barbot, S., Peltzer, G., Doin, M.-P., Liu, Z. & Jolivet, R., 2016. Constraining the kinematics of metropolitan Los Angeles faults with a slip-partitioning model, *Geophys. Res. Lett.,* **43,** 11 192–111 201.

Delacou, B., Sue, C., Champagnac, J.-D. & Burkhard, M., 2004. Present-day geodynamics in the bend of the western and central Alps as constrained by earthquake analysis, *Geophys. J. Int.,* **158**(2), 753–774.

Delacou, B., Sue, C., Champagnac, J.D. & Burkhard, M., 2005. Origin of the current stress field in the western/central Alps: role of gravitational re-equilibration constrained by numerical modelling, *Geol. Soc. Lond., Spec. Publ.,* **243**(1), 295–310.

Delacou, B., Sue, C., Nocquet, J.M., Champagnac, J.D., Allanic, C. & Burkhard, M., 2008. Quantification of strain rate in the Western Alps using geodesy: comparisons with seismotectonics, *Swiss J. Geosci.,* **101**(2), 377–385.

Hannouz, E., 2019. *Quantification des taux de déformation sismique dans la zone de transfert tectonique des Alpes à la Vallée du Rhône,* Master thesis, University Grenoble Alpes, Grenoble.

Herring, T.A., King, R.W., Floyd, M.A. & McClusky, S.C., 2015. *Introduction to GAMIT/GLOBK, Release 10.6, Mass*. Institute of Technology, Cambridge.

Lyard, F., Lefevre, F., Letellier, T. & Francis, O., 2006. Modelling the global ocean tides: modern insights from FES2004, *Ocean Dyn.,* **56**(5–6), 394–415.

Manchuel, K., Traversa, P., Baumont, D., Cara, M., Nayman, E. & Durouchoux, C., 2018. The French seismic CATalogue (FCAT-17), *Bull. Earthq. Eng.,* **16**(6), 2227–2251.

Marinière, J., Nocquet, J.-M., Beauval, C., Champenois, J., Audin, L., Alvarado, A., Baize, S. & Socquet, A., 2019. Geodetic evidence for shallow creep along the Quito fault, Ecuador, *Geophys. J. Int,* doi:10.1093/gji/ggz564.

Masson, F., Lehujeur, M., Ziegler, Y. & Doubre, C., 2014. Strain rate tensor in Iran from a new GPS velocity field, *Geophys. J. Int.,* **197**(1), 10–21.

McCaffrey, R., 2009. Time-dependent inversion of three-component continuous GPS for steady and transient sources in northern Cascadia, *Geophys. Res. Lett.,* **36,** doi:10.1029/2008GL036784.

Mousavi, Z., Walpersdorf, A., Walker, R.T., Tavakoli, F., Pathier, E., Nankali, H.R.E.A. & Djamour, Y., 2013. Global Positioning System constraints on the active tectonics of NE Iran and the South Caspian region, *Earth planet. Sci. Lett.,* **377,** 287–298.

Nguyen, H., Vernant, P., Mazzotti, S., Khazaradze, G. & Asensio Ferreira, E., 2016. 3D GPS velocity field and its implications on the present-day postorogenic deformation of the Western Alps and Pyrenees, *Solid Earth,* **7,** 1349–1363.

Nocquet, J.M. *et al.*, 2016. Present-day uplift of the western Alps, *Sci. Rep.,* **6,** 28404. doi:10.1038/srep28404.

Pinget, L., 2016. *Le champ de deformation 3D des Alpes occidentales par 20 ans de données GNSS,* Master thesis, University Grenoble Alpes, Grenoble.

Reilinger, R. *et al.*, 2006. GPS constraints on continental deformation in the Africa-Arabia-Eurasia continental collision zone and implications for the dynamics of plate interactions, *J. geophys. Res.,* **11**(B5), doi:10.1029/2005JB004051.

RESIF, 2017. RESIF-RENAG French national Geodetic Network. RESIF—Réseau Sismologique et géodésique français. Available at: https://doi.org/10.15778/resif.rg, (last accessed 05/06/2020).

Sánchez, L., Ch, V., Sokolov, A., Arenz, H. & Seitz, F., 2018. Present-day surface deformation of the Alpine region inferred from geodetic techniques, *Earth Syst. Sci. Data,* **10**(3), 1503–1526.

Segall, P., 2010. *Earthquake and Volcano Deformation,* Princeton Univ. Press, 456pp.

Shen, Z.K., Wang, M., Zeng, Y. & Wang, F., 2015. Optimal interpolation of spatially discretized geodetic data, *Bull. seism. Soc. Am.,* **105**(4), 2117–2127.

Shewchuk, J.R., 1996. Triangle: Engineering a 2D quality mesh generator and Delaunay triangulator, in *Workshop on Applied Computational Geometry,* pp. 203–222, Springer, Berlin, Heidelberg.

Stampfli, G.M., Borel, G.D., Marchant, R. & Mosar, J., 2002. Western Alps geological constraints on western Tethyan reconstructions, *J. Virtual Explorer,* **8,** pp. 75–104.

Sternai, P., Sue, C., Husson, L., Serpelloni, E., Becker, T.W., Willett, S.D. & Valla, P., 2019. Present-day uplift of the European Alps: evaluating mechanisms and models of their relative contributions, *Earth Sci. Rev.*, vol. 190, pp. 589-604, doi:10.1016/j.earscirev.2019.01.005.

Sue, C. & Tricart, P., 1999. Late alpine brittle extension above the Frontal Pennine Thrust near Briançon, western Alps, *Eclogae Geol. Helv.,* **92**(2), 171–181.

Sue, C., Thouvenot, F., Fréchet, J. & Tricart, P., 1999. Widespread extension in the core of the western Alps revealed by earthquake analysis, *J. geophys. Res.: Solid Earth,* **104**(B11), 25611–25622.

Sue, C., Martinod, J., Tricart, P., Thouvenot, F., Gamond, J.F., Fréchet, J. & Grasso, J.R., 2000. Active deformation in the inner western Alps inferred from comparison between 1972-classical and 1996-GPS geodetic surveys, *Tectonophysics,* **320**(1), 17–29.

Sue, C. & Tricart, P., 2002. Widespread post-nappe normal faulting in the Internal Western Alps: a new constraint on arc dynamics, *J. geol. Soc.,* **159**(1), 61–70.

Sue, C. & Tricart, P., 2003. Neogene to ongoing normal faulting in the inner western Alps: a major evolution of the alpine tectonics, *Tectonics,* **22,** 1–25.

Sue, C., Delacou, B., Champagnac, J.D., Allanic, C., Tricart, P. & Burkhard, M., 2007a. Extensional neotectonics around the bend of the Western/Central Alps: an overview, *Int. J. Earth Sci.,* **96**(6), 1101–1129.

Sue, C., Delacou, B., Champagnac, J.D., Allanic, C. & Burkhard, M., 2007b. Aseismic deformation in the Alps: GPS vs. seismic strain quantification, *Terra Nova,* **19**(3), 182–188.

Schwartz, S., Guillot, S., Tricart, P., Bernet, M., Jourdan, S., Dumont, T. & Montagnac, G., 2012. Source tracing of detrital serpentinite in the Oligocene molasse deposits from the western Alps (Barrême basin): implications for relief formation in the internal zone, *Geol. Mag.,* **149**(5), 841–856.

Tarayoun, A., 2018. *Localisation de la déformation et de la sismicité en domaine intraplaque: réactivation des paléo-structures crustales et lithosphériques,* PhD thesis, Université de Montpellier, Montpellier.

Tregoning, P. & van Dam, T., 2005. Atmospheric pressure loading corrections applied to GPS data at the observation level, *Geophys. Res. Lett.,* **32**(22), doi:10.1029/2005GL024104.

Tricart, P., Lardeaux, J.M., Schwartz, S. & Sue, C., 2006. The late extension in the inner western Alps: a synthesis along the south-Pelvoux transect, *Bull. géol. Soc. France,* **177**(6), 299–310.

Tricart, P., 1984. From passive margin to continental collision; a tectonic scenario for the Western Alps, *Am. J. Sci.,* **284**(2), 97–120.

Vernant, P., Nilforoushan, F., Hatzfeld, D., Abbassi, M.R., Vigny, C., Masson, F. & Tavakoli, F., 2004. Present-day crustal deformation and plate kinematics in the Middle East constrained by GPS measurements in Iran and northern Oman, *Geophys. J. Int.,* **157**(1), 381–398.

Vernant, P., Hivert, F., Chery, J., Steer, P., Cattin, R. & Rigo, A., 2013. Erosion-induced isostatic rebound triggers extension in low convergent mountain ranges, *Geology,* **41**(4), 467–470.

Walpersdorf, A. *et al.*, 2015. Coherence between geodetic and seismic deformation in a context of slow tectonic activity (SW Alps, France), *J. Geodyn.,* **85,** 58–65.

Walpersdorf, A., Pinget, L., Vernant, P., Sue, C. & Deprez, A. RENAG team, 2018. Does long-term GPS in the Western Alps finally confirm earthquake mechanisms?, *Tectonics,* **37**(10), 3721–3737.

Ward, S.N., 1994. A multidisciplinary approach to seismic hazard in southern California, *Bull. seism. Soc. Am.,* **84**(5), 1293–1309.

SUPPORTING INFORMATION

Supplementary data are available at *GJI* online.

Supplementary 1. Table of data acquisitions.

Supplementary 2. Table of velocities and uncertainties used in the study.

Supplementary 3. Data combination to derive the velocity field.

Table S3. Mean east (Ve), north (Vn) and total differences of stations' velocities on each side of the Durance fault for the four velocity fields.

Figure S3. Δv per station (red dots) and $X\Delta v$ (grey line) representing global coherence between two velocity fields. The green line stands for the standard deviation (1σ). (a) Coherence between local tie and equated solutions. (b) Coherence between local tie and bolt marks solutions. (c) Coherence between local tie and screw marks solutions.

Please note: Oxford University Press is not responsible for the content or functionality of any supporting materials supplied by the authors. Any queries (other than missing material) should be directed to the corresponding author for the paper.